

# Experimental investigation of the impact of porous parameters on trailing-edge noise

Minghui Zhang\*

*Shandong University of Science and Technology, Qingdao, Shandong Province, 266590, China*

Tze Pei Chong

*Brunel University London, Uxbridge, UB8 3PH, United Kingdom*

This paper presents a sensitivity and parametric study of the sound generation at the non-tortuous and wall-normal permeable trailing edge of an aerofoil. Design parameters for the porous properties include the porosity, pore-size and porous-coverage. For a combination of large pore-size, small porosity and large porous-coverage, wake vortex shedding is likely to be triggered, and either sharp tone or broadened tone will dominate the radiated field. Using the appropriate hydrodynamic and geometrical length scales, the radiated spectra for the tones are found to follow the Strouhal number relationship, thus allow a reasonably accurate prediction of the primary tone frequency. These extraneous tones can potentially undermine the current porous trailing edge concept. Still, they can also be avoided if the porous parameters are mostly of small pore-size (sub-millimetre), medium to large porosity or small porous-coverage. Under these porous settings, better spatially distributed permeable air will seep through the surface and disrupt the generation mechanism of the turbulent boundary layer, which then translate into a lower level of turbulent broadband noise radiation. The most optimised non-tortuous, wall-normal permeable trailing edge tested in the current study can achieve a maximum of 7 dB reduction for the turbulent broadband noise. Considering that the primary trailing edge noise source is situated very near to the edge, a targeted approach (i.e. small porous-coverage) is already sufficient to achieve significant trailing edge broadband noise reduction.

**Keywords:** aerofoil self-noise, porous trailing edge, additive manufacturing, wall-normal permeability

\* Corresponding author

E-mail: [zmh1999238@163.com](mailto:zmh1999238@163.com) (M.H. Zhang); [t.p.chong@brunel.ac.uk](mailto:t.p.chong@brunel.ac.uk) (T. P. Chong)

# 1. Introduction

Strong market demand for quieter aircraft encourages the aviation industries to continue their investments to develop quieter airframes and turbo engines [1]. For this reason, passive and active noise reduction techniques, such as the use of the unique features found on the wings of owls, show great potential [2–5]. These can be in the forms of self-noise reduction by the trailing edge serrations [6–9], or turbulence-interaction noise reduction by the leading edge serration [10–12]. Hybrid method is also used to enhance the reduction of trailing edge noise, such as the poro-serrated trailing edge [13, 14], or the combed-serrated trailing edge [15]. Active flow control [16, 17] represents another avenue to achieve aerofoil noise reduction, although the complexity in operation and extra power demand will make it less attractive for an eventual adoption by the industries.

Another solution in the passive control field is the use of porous, flow-permeable materials. There are many investigations aiming at porous or partly porous aerofoil to achieve aerofoil noise reduction. Geyer *et al.* [18–20] constructed several fully porous SD7003 aerofoils that have different flow resistivities. After performing extensive acoustic measurements, the potential to reduce trailing edge noise has been confirmed. It is found that the level and characteristic of the noise reduction depend on the flow resistivity, and to some extents, the porosity. Unfortunately, the low-noise benefit of a fully porous aerofoil is negated by the deterioration in the aerodynamics performances. For example, they observe that a porous aerofoil can reduce up to 80% of the lift coefficient, and increase the drag coefficient up to 10 folds. Partially porous aerofoil represents an alternative design that can minimise the aerodynamics penalty and preserve the low-noise characteristic. Geyer and Sarradj [21] limit the porous coatings to the last 5% of the chord length from the trailing edge, where they still can observe a reduction in the far-field noise up to 8 dB and a negligible reduction in the lift coefficient. Herr *et al.* [22] tested a DLR F16 aerofoil with different permeable materials trailing edge. They report that noise reduction mostly occurs at lower frequencies. Further study on the flow permeability of porous trailing edge has been conducted by Carpio *et al.* [23]. They manufacture two types of porous trailing edges, both of which cover the last 20% of the chord. These two porous trailing edges are represented by separate metal foams with cell diameters of 450 and 800  $\mu\text{m}$ , respectively. They observe that the permeability of the porous inserts can increase the anisotropy level of the highly energetic turbulent motion. The resulting manipulation of the turbulent boundary layer yields up to 11 dB noise reduction when the porous insert has a high flow permeability. Using a high-resolution large-eddy simulation/computational aeroacoustics (LES/CAA) approach, Koh *et al.* [24, 25] study the impact of porous material with different properties on the trailing edge noise radiation. It is shown that the viscous dissipation in the porous structures can directly affect the level of the acoustical attenuation. The main mechanism is related to the reduction of the turbulent eddies correlation length by the flow acceleration near the trailing edge. Zhou *et al.* [26] develop a discrete

adjoin framework with porous media. Based on the algorithmic differentiation for trailing edge noise minimisation, they can predict a maximum noise reduction of 12 dB from a flat plate trailing edge. Hedayati *et al.* [27] manufacture their trailing edge with the open-cell Ni-Cr-Al foam. This type of metal foam is characterised by sub-millimetre pore size. They obtain encouraging results in the reduction of the broadband trailing edge noise.

Due to the complexity involved in the manufacturing process, most of the porous materials can only be procured commercially by the researchers. However, the porosity, flow resistivity and permeability levels of the commercially-graded porous materials are usually pre-fixed. This makes a thorough study on the aeroacoustics performance by the porous trailing edge a difficult task. In addition, even the same grade and type of porous materials can have inhomogeneous internal pore structure and permeability tensors between the samples. This inconsistency can complicate any attempts to generalise the porous aerofoils in their noise reduction performance. Recently, the rapid advances of the additive manufacturing technique, such as the 3D-printing [28], could be used for the manufacturing of the permeable trailing edge with high accuracy. The most straightforward configuration is to connect the suction and pressure sides of the aerofoil with straight channels, such as the propeller blades adopted in [29]. Carpio *et al.* [30] measure the far-field noise radiated by a NACA0018 aerofoil retrofitted with solid and 3D-printed permeable trailing edge inserts at the last 20% of the chord. It is observed that the 3D-printed inserts must be at least 3 times as permeable as the commercial metal foam in order to obtain a similar broadband noise reduction level. Wang [31] investigates the noise abatement through porous trailing edge treatment to the forward rotor propeller where 6–7 dB overall sound pressure level reduction is achieved without incurring much aerodynamic penalty. Sumesh *et al.* [32] design a configuration with a single line distribution of 3 mm diameter holes adjacent to the trailing edge of their aerofoil. The results indicate that the treated aerofoil is effective in the reduction of the lower frequency noise ( $< 3.5$  kHz).

In most of the previous studies, the effects of permeable materials, pore characteristics, flow resistivity and amount of porous treatment to the trailing edge have mostly been studied respectively, but not interactively. As part of efforts to fill the knowledge gap, the effect of straight channel permeable trailing edge on the aerofoil self-noise manipulation represents the focus of this work. The permeable trailing edges studied here are defined by their porosity, pore-size, and porous-coverage (the percentage of porous treatment). These parameters can be controlled accurately in the design stage through the computer-aided design package. During the manufacturing stage, various porous trailing edges can be 3D-printed in high precision by a Stereolithography (SLA) 3D-printer. The aim of this paper is to present a parametric and sensitivity study on the aeroacoustics behaviours of aerofoil with wall-normal permeable trailing edges. Some interesting aeroacoustics behaviours are uncovered, which have not yet been reported extensively in the literatures. Some of the acoustic spectra will be presented with non-dimensional frequency to allow comparison of the data, as well as extraction of the noise-generation mechanisms.

## 2. Experimental set-up

### 2.1 Aerofoil model and the design of wall-normal permeable trailing edges

The aerofoil is an asymmetric, highly cambered NACA 65(12)-10, with a nominal chord length  $c = 150$  mm and span  $L = 300$  mm. It is equipped with 22 pressure taps exposed at the suction and pressure sides up to 80% of the chord. A schematic of the aerofoil model is shown in Fig. 1. The model is 3D-printed by a Viper Si2 SLA additive manufacturing system. It has an interchangeable section at the rear to allow the insertion of different porous trailing edges, including the solid reference configuration, to the main body to form a complete aerofoil model. The laboratory coordinate system is denoted by  $X$ ,  $Y$  and  $Z$ , which refer to the streamwise, wall-normal and spanwise directions, respectively. Note that  $Z = 0$  is located at the mid-span plane of the aerofoil, where  $X = 0$  originates from the trailing edge. The aerofoil body is therefore situated at the negative  $X$  region. For example, a streamwise location of 130 mm from the leading edge is represented by  $X = -20$  mm.  $Y = 0$  locates at the trailing edge, where a positive  $Y$  refers to the suction side, and a negative  $Y$  is at the pressure side. This coordinate system is employed throughout the paper. A symbol  $\psi$  is defined here to represent the percentage of porous-coverage at the trailing edge. The porous trailing edge inserts would normally cover between  $X = -30$  and 0 mm (equivalent to  $-0.2 \leq X/c \leq 0$ , or  $\psi = 20\%$ , see Fig. 1) to ensure that there is enough treated surface to manipulate the turbulent boundary layer. However,  $\psi$  with values other than 20% will also be investigated for their effect on the radiated noise spectra.

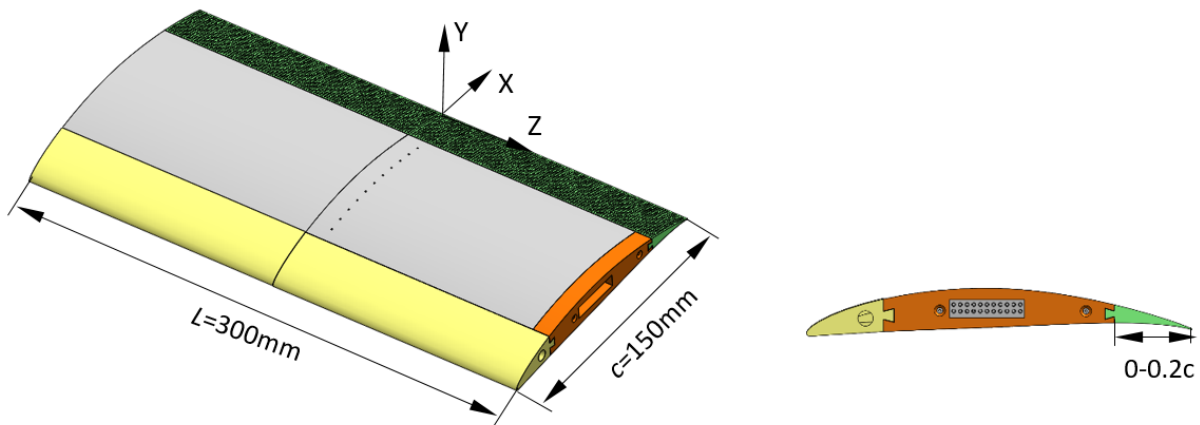


**Fig. 1.** Perspective view and side view of the NACA 65(12)-10 model

In total, there are large number of porous trailing edges investigated in the current study. These are the products of different combination of porosity, pore-size, and porous-coverage. The solid baseline trailing edge is tested under the same flow condition and pressure loadings as the porous trailing edge cases to allow a meaningful comparison of their aeroacoustics performances. Detailed descriptions of these porous trailing edges are summarised in [Tables 1–3](#).

In the first set of test, a matrix of (3 x porosities) and (3 x pore-sizes), resulting in total of 9 porous trailing edges, was investigated. Note that these porous trailing edges all employ a rectilinear pore-pattern, circular pore-shape and  $\psi = 20\%$ . An example of the porous sample produced by the SLA 3D-printer is shown in [Fig. 2a](#). The rectilinear pattern of the pore design is depicted in [Fig. 2b](#). The porosity is controlled by the pore-size (diameter  $d$ ), streamwise distance between adjacent pores  $t$ , and spanwise distance  $h$ . Here  $d = 1, 2$  and  $3$  mm, and the porosity  $\sigma = 20, 30$  and  $40\%$ . The porosity  $\sigma$  is defined as:

$$\sigma = V_{pore} / V_{total} \quad (1)$$

$V_{pore}$  is the cumulative volume of the pores, and  $V_{total}$  is the total/bulk volume of the treated trailing edge. To make it easier to differentiate the trailing edge devices, they are named according to the values of  $\sigma$  and  $d$ . [Table 1](#) summaries the geometrical parameters of the above trailing edge devices. Note that, unless explicitly stated, the naming of the individual porous trailing edge always takes a default porous-coverage  $\psi = 20\%$ . For example, a porous trailing edge with  $\sigma = 30\%$ ,  $d = 1$  mm and  $\psi = 20\%$  will be named as 30%–1mm. Configuration that has different porous-coverage will be specified in the bracket following the name. For example, 30%–1mm ( $\psi = 13.7\%$ ) refers to the 30%–1mm with 13.7% of porous-coverage, and so on.

**Table 1** Porous trailing edges with different pore-size and porosity

Symbols	Pore-shape	$d$ (mm)	$t$ (mm)	$h$ (mm)	$\sigma$	$\psi$
20%–1mm	circular	1.0	2.0	1.9	20%	20%
30%–1mm	circular	1.0	1.5	1.6	30%	20%
40%–1mm	circular	1.0	1.3	1.4	40%	20%
20%–2mm	circular	2.0	4.2	4.6	20%	20%
30%–2mm	circular	2.0	3.2	3.1	30%	20%
40%–2mm	circular	2.0	2.6	2.8	40%	20%
20%–3mm	circular	3.0	6.0	5.8	20%	20%
30%–3mm	circular	3.0	4.8	4.7	30%	20%
40%–3mm	circular	3.0	4.0	4.0	40%	20%

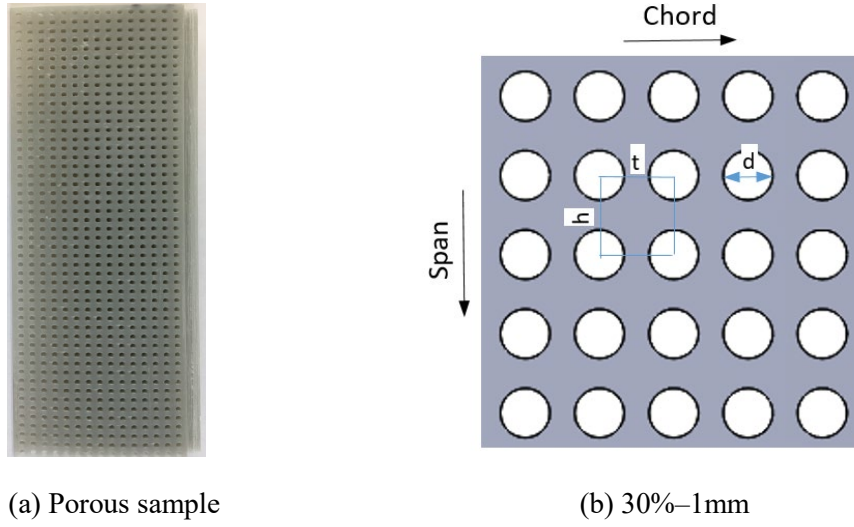


**Fig. 2.** (a) Sample of the 3D-printed porous trailing edge, and (b) patterns of the pore designs

The second set of test focuses on the effect of the porous-coverage to the radiated trailing edge noise. Essentially, with a constant porosity, the level of porous-coverage as depicted in Fig. 3 correlates to the level of porous treatment in the trailing edge. In total, 17 different levels of porous-coverage, all of which are configured by  $d = 1$  mm,  $\sigma = 30\%$ ,  $t = h = 1.5$  mm, circular pore-shape and rectilinear pore-pattern, are investigated for their aeroacoustics behaviours. Note that the porous-coverage starts from the trailing edge and moves upstream.  $\psi = 3.7\%$  refers to porous-coverage between  $X = 0$  and  $-5.5$  mm, whereas  $\psi = 4.7\%$  refers to porous-coverage between  $X = 0$  and  $-7.0$  mm, and so on. It is important to note that each configuration will encounter different pore-depth, i.e. the larger the value of  $\psi$ , the larger the pore-depth will be. Later, this relationship is found to be the deciding factor for the triggering of the vortex shedding in the wake. Summary of the geometrical parameters of these porous trailing edges are given in [Table 2](#).

The third test is to investigate the effect of very small pore-size (sub-millimetre) on the porous trailing edge aeroacoustics performance. Taking into account of the limitation of the in-house 3D printer, we settle for the diameter of  $d = 0.6$  mm with a porosity of  $\sigma = 30\%$  and porous-coverage of  $\psi = 20\%$ . The geometrical parameters are given in [Table 3](#). Note that the experimental works from [[18-21](#), [23](#)] are also based on the porous materials of small pore-size, which are typically less than 1 mm in the cell diameter.

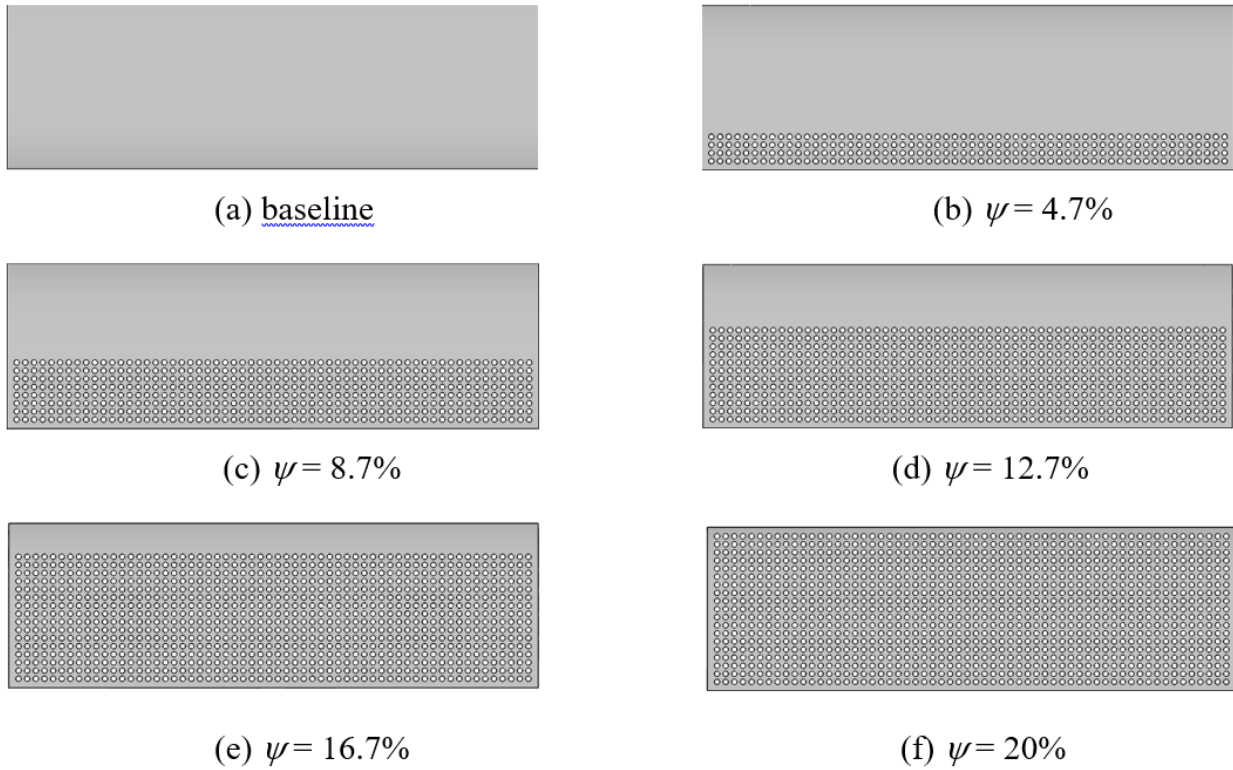


**Fig. 3.** Some schematic examples illustrating the different levels of porous-coverage  $\psi$  to the aerofoil trailing edge

**Table 2** Porous trailing edges of different porous-coverage

Symbols	Pore-shape	$d$ (mm)	$t$ (mm)	$h$ (mm)	$t_h$ (mm)	$\sigma$	$\psi$
30%–1mm ( $\psi = 3.7\%$ )	circular	1.0	1.5	1.6	1.25	30%	3.7%
30%–1mm ( $\psi = 4.7\%$ )	circular	1.0	1.5	1.6	1.54	30%	4.7%
30%–1mm ( $\psi = 5.7\%$ )	circular	1.0	1.5	1.6	1.85	30%	5.7%
30%–1mm ( $\psi = 6.7\%$ )	circular	1.0	1.5	1.6	2.17	30%	6.7%
30%–1mm ( $\psi = 7.7\%$ )	circular	1.0	1.5	1.6	2.50	30%	7.7%
30%–1mm ( $\psi = 8.7\%$ )	circular	1.0	1.5	1.6	2.84	30%	8.7%
30%–1mm ( $\psi = 9.7\%$ )	circular	1.0	1.5	1.6	3.18	30%	9.7%
30%–1mm ( $\psi = 10.7\%$ )	circular	1.0	1.5	1.6	3.52	30%	10.7%
30%–1mm ( $\psi = 11.7\%$ )	circular	1.0	1.5	1.6	3.87	30%	11.7%
30%–1mm ( $\psi = 12.7\%$ )	circular	1.0	1.5	1.6	4.23	30%	12.7%
30%–1mm ( $\psi = 13.7\%$ )	circular	1.0	1.5	1.6	4.58	30%	13.7%
30%–1mm ( $\psi = 14.7\%$ )	circular	1.0	1.5	1.6	4.94	30%	14.7%
30%–1mm ( $\psi = 15.7\%$ )	circular	1.0	1.5	1.6	5.30	30%	15.7%
30%–1mm ( $\psi = 16.7\%$ )	circular	1.0	1.5	1.6	5.67	30%	16.7%
30%–1mm ( $\psi = 17.7\%$ )	circular	1.0	1.5	1.6	6.03	30%	17.7%
30%–1mm ( $\psi = 18.7\%$ )	circular	1.0	1.5	1.6	6.39	30%	18.7%
30%–1mm ( $\psi = 20\%$ )	circular	1.0	1.5	1.6	6.75	30%	20.0%

**Table 3** A sub-millimeter porous trailing edge

Symbols	Pore-shape	$d$ (mm)	$t_1$ (mm)	$t_2$ (mm)	$h_1$ (mm)	$h_2$ (mm)	$\sigma$	$\psi$
30%–0.6mm	circular	0.6	0.65	0.65	0.66	0.66	30%	20%

## 2.2 Wind tunnel and acoustic measurements

Noise measurements are conducted in an aeroacoustics open jet wind tunnel at Brunel University London. The open jet wind tunnel is situated in a  $4 \times 5 \times 3.4$  m anechoic chamber, and is suitable to measure the far-field radiation of the aerofoil self-noise. The nozzle exit is rectangular with dimensions of 0.1 m (height)  $\times$  0.3 m (width). This wind tunnel can achieve a turbulence intensity of between 0.1% and 0.2% and a maximum jet velocity of about  $80 \text{ ms}^{-1}$ . The aerofoil model is held by side plates, which can be used to adjust the angle of attack and the position of the aerofoil with respect to the nozzle axis of the

wind tunnel. Above the aerofoil, there are eight condenser microphones (G.R.A.S. 46AE, ½” Constant Current Power free-field) at polar angles of  $50^\circ \leq \theta \leq 120^\circ$  (interval of  $10^\circ$ ) at the mid-span location of the trailing edge. The separation distance between these microphones and the trailing edge is 1 m. A piston phone from G.R.A.S. 42AB (sounds pressure level 114 dB at 1 kHz) is used to calibrate these microphones. Data acquisition is facilitated by a National Instrument 16-bit Analogue-to-Digital card at 44 kHz sampling rate over 15 seconds sampling time. The acquired data is then windowed and the Power Spectral Density of 1 Hz narrowband bandwidth and a frequency resolution of 43 Hz is subsequently calculated using a 1024-point Fast Fourier Transform.

Prior to the measurement of the aerofoil noise, background noise of the wind tunnel (without the presence of the aerofoil, but with the side-plates attached) is measured between  $20$  and  $60 \text{ ms}^{-1}$  (interval of  $2 \text{ ms}^{-1}$ ). The same speed range is then repeated, corresponding to Reynolds numbers  $2 \times 10^5$  and  $6 \times 10^5$ , respectively, when the aerofoil model is installed to the wind tunnel side-plates. In the experiment, boundary layer trip elements were placed at a streamwise location of 20 mm from the leading edge on both sides of the aerofoil in order to achieve a fully turbulent boundary layer condition at the trailing edge.

### 2.3 Particle Image Velocimetry

The velocity field near the porous trailing edge of the aerofoil is also measured by the Particle Image Velocimetry (PIV) technique. The PIV system includes a source that generates a double pulse laser beam (Litron® Nd:YAG-Laser) with maximum output energy of 200 mJ. The laser beam has a diameter of 5 mm that can be expanded through a set of lenses. The maximum pulsing frequency is 15 Hz. A CCD camera (FlowSense EO 2M) is used to capture the images of the flow domain at 44 frames/second with an output resolution of  $1600 \times 1200$  pixel on size of 7.4 mm.

For the porous trailing edges 30%–1mm, 30%–2mm, 30%–0.6mm, as well as the baseline solid trailing edge, the PIV experiments are performed in the longitudinal and wall-normal plane ( $X - Y$ ) at the mid span of the aerofoil. The experimental setup is depicted in Fig. 4a. The field of view is shown in Fig. 4b on the gray area, which covers  $0.4c \times 0.5c$  ( $60 \times 75 \text{ mm}^2$ ). The measured area after the trailing edge is confined between  $0.0 \leq X/c \leq 0.4$  in the longitudinal direction and  $-0.2 \leq Y/c \leq 0.3$  in the wall-normal direction.

During the data analysis, the spanwise vorticity and velocity fluctuations are calculated from approximately 1500 images.

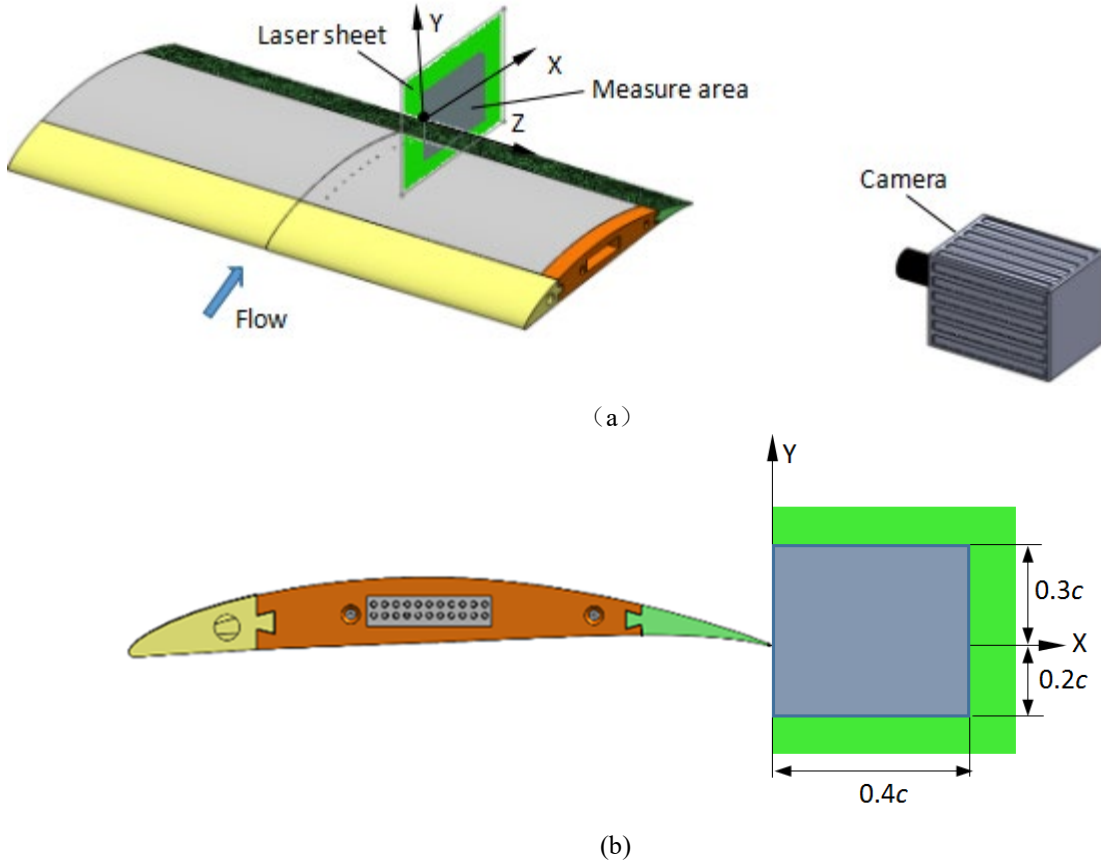


**Fig. 4.** (a) Schematic of the PIV setup. (b) Detail of the measured area and coordinate system

#### 2.4 Experimental data processing and numerical simulation of the baseline aerofoil

Assuming a cylindrical radiation, radiation from an aerofoil trailing edge more closely resembles a line source than a point source. The sound power level  $PWL$  per unit span can be calculated by Eq. (2).

$$W(f) = \frac{2\pi r \sum_i^n \phi_{pp}(f, \theta_i) \Delta\theta}{\rho c_o} \quad i = 1, 2, \dots, 8 \quad ; \quad 50^\circ \leq \theta \leq 120^\circ \quad (2)$$

$$PWL(f) = 10 \log_{10} \left[ \frac{W(f)}{W_o} \right] \quad W_o = 10^{-12} W / Hz$$

where  $W(f)$  is the sound power integrated between the radiation angles  $50^\circ \leq \theta \leq 120^\circ$ .  $\phi_{pp}(f, \theta)$  is the acoustic pressure spectrum density measured by microphone  $i$ ,  $n$  is the number of the microphones,  $r$  is the distance between the aerofoil trailing edge and the microphones,  $\Delta\theta = 10^\circ \times \pi/180^\circ$  is the radian angle between adjacent microphones,  $c_o$  is the speed of sound and  $\rho$  is the air density.

The reduction in the sound power level ( $\Delta PWL$ ) is expressed as the difference between the sound power level radiated by the porous aerofoil, and the sound power level radiated by the baseline aerofoil, as shown in the Eq. (3).

$$\Delta PWL(f) = PWL_{porous}(f) - PWL_{baseline}(f) \quad (3)$$

In some of the  $\Delta PWL$  graphs, they are plotted against the Strouhal number ( $S_{tr}$ ), with the length scale represented by the turbulent boundary layer displacement thickness ( $\delta^*$ ) at the trailing edge. The definition of  $\delta^*$  will be provided later. With  $U_o$  representing the inflow velocity, the  $S_{tr}$  is defined by:

$$S_{tr} = \frac{f \delta^*}{U_o} \quad (4)$$

To implement Eq. (4), the turbulent boundary layer displacement thicknesses  $\delta^*$  developed on the aerofoil surfaces at each  $U_o$  need to be known. Due to a large range of  $U_o$  needed to investigate in the current study, it is not feasible to measure experimentally of all the  $\delta^*$  values on both the suction and pressure sides of the aerofoil. Instead, the values are numerically calculated by the commercial software FLUENT based on the turbulence modelling of the flow field. However, considering that the inflow is supplied through a rather narrow nozzle, the pressure loading experienced by the aerofoil in an open jet configuration could be different compared to the case when the aerofoil is immersed in a large potential flow domain. This could affect the prediction of the turbulent boundary layer properties. To take into account of this effect in the numerical modelling, the open jet velocity profile measured at the nozzle outlet is used as the inlet boundary condition. The overall computation zone is shown in Fig. 5a. As mentioned previously, the inlet condition is determined by the measured velocity profile (with the aerofoil presence), which is shown in Fig. 5b for an inlet velocity  $U_o = 24 \text{ ms}^{-1}$ . The outlet is designed as a pressure outlet, which equals to the atmospheric pressure. Others boundaries are defined as the solid wall surfaces.

Bypass transition of the boundary layer on the aerofoil surfaces is numerically triggered by protrusion as the geometrical discontinuity, as shown in Fig. 5c. The relative complexity in this type of aerofoil geometry calls for a careful definition of the grid layout. The calculated area is divided into 13 grid regions. The node number of the grid is set to 50 x 20 at the inlet area, whereas at the exit it is set to 100 x 20 nodes. There are 150 nodes in the streamwise direction on the upper and lower surfaces of the aerofoil. In order to predict the mean properties of the turbulent boundary layer with a reasonable accuracy, the first layer of the grid height with relative to the aerofoil surface is about 3.5  $\mu\text{m}$ , which typically results in the wall-unit of  $y^+ < 1$  at the trailing edge region. The mesh layout adopted in this study is shown in Fig. 5c.

As mentioned in the previous paragraph, a bypass transition has to be triggered in the numerical simulation. This is done by protruding physical steps of the same height as the tripping element used in the experiment, on both sides of the aerofoil, to “trip” the boundary layers numerically. Except at the location of the tripping, comparison of the pressure coefficients  $C_p$  between the numerical and experimental results is excellent, as demonstrated in Fig. 5d.

In order to evaluate the grid independence on the calculated results, three different grid density defined as the total number of grid nodes:  $2.4 \times 10^5$  (case 1),  $3.9 \times 10^5$  (case 2), and  $5.8 \times 10^5$  (case 3), are calculated under the condition that the  $y^+ < 1$  is met at the trailing edge. Using the Transition  $\kappa$ - $\omega$  SST turbulence model, Fig. 6a and 6b show the variations of the boundary layer displacement thickness  $\delta^*$  on the aerofoil suction and pressure surfaces for the three cases, each of which is calculated at the chord length  $0.9c$  at five different inflow velocities  $U_o$ . It is shown that the discrepancies between the case 2 and case 3 are minimal. In order to have a more effective use of the computational time, the numerical grid scheme pertaining to the case 2 is chosen throughout this study.

In this study, the Strouhal number ( $S_{tr}$ ) is determined from the turbulent boundary layer displacement thickness  $\delta^*$  of the aerofoil at  $0.9c$ . The  $\delta^*$  is defined in Eq. (5), where  $\delta_1^*$  and  $\delta_2^*$  are the turbulent boundary layer displacement thickness at the suction and pressure sides, respectively (see Fig. 7a). The variation of  $\delta^*$  at  $0.9c$  across the inlet velocity  $U_o$  is shown in Fig. 7b.

$$\delta^* = \frac{\delta_1^* + \delta_2^*}{2} \quad (5)$$

Comparison of the boundary layer thickness  $\delta$  and the displacement thicknesses  $\delta^*$  between the numerical and experimental results is shown in Table. 4. Note that the experimental results are obtained by a separate hot wire measurement. Although this verification study is for one particular inflow condition only, the acceptable level of agreement lends some confidences to the numerical results obtained in the current study.

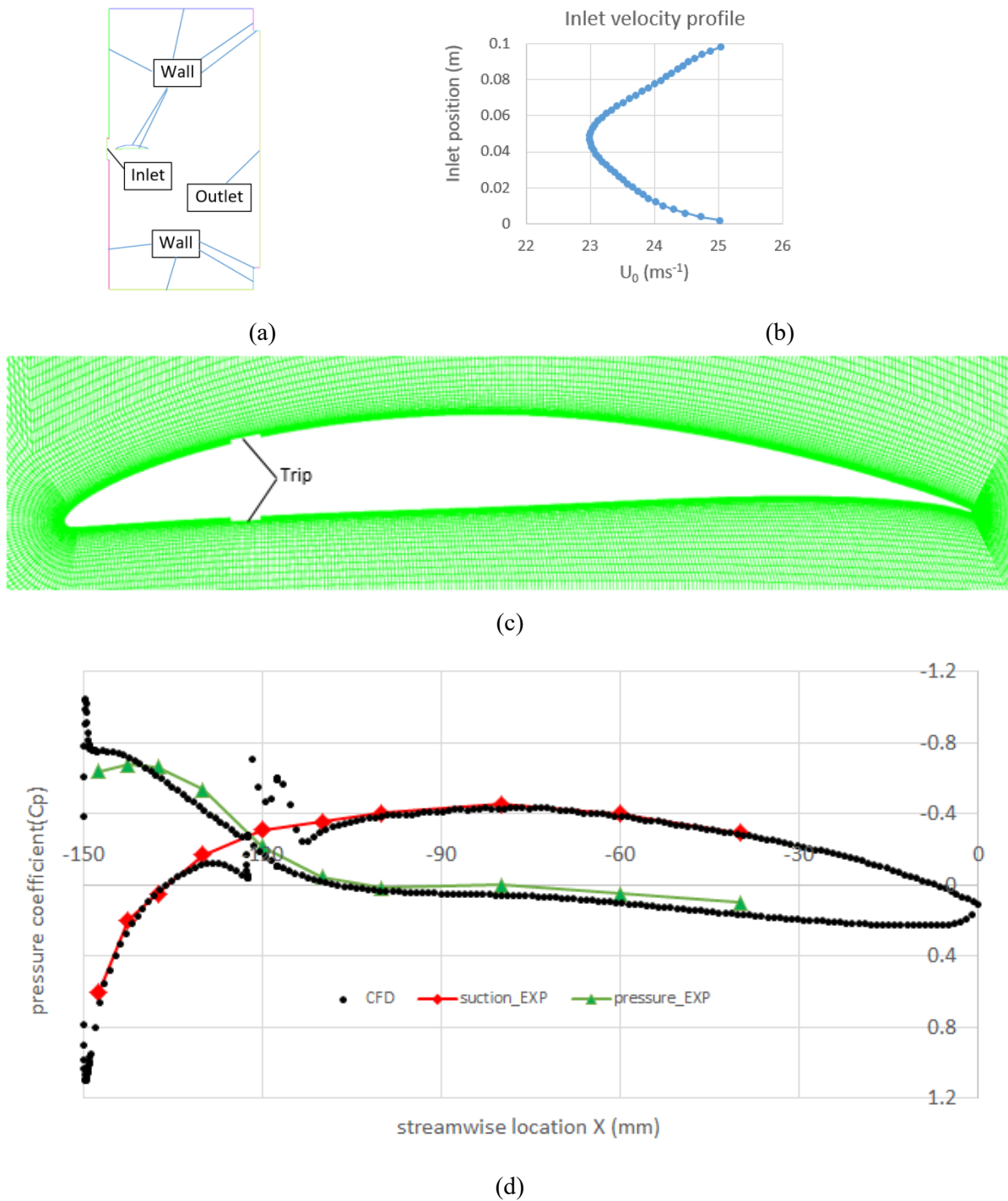
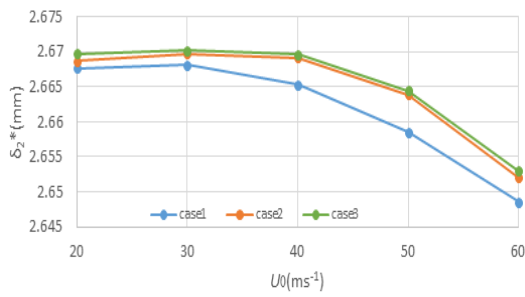


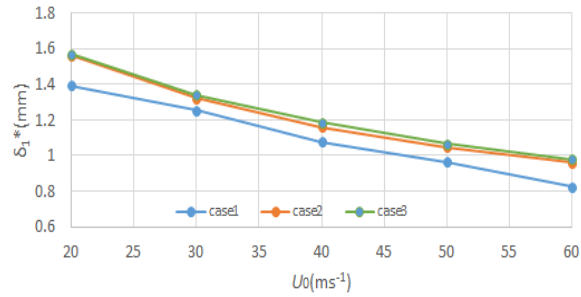
**Fig. 5.** (a) Computation zone for the RANS, (b) measured inlet velocity profile after the nozzle exit (applied to the “inlet” in (a)), (c) zoomed-in mesh grid distribution for the numerical simulations, and (d) comparison of the pressure coefficients between the numerical and experimental results

**Table 4** Comparison of the boundary layer mean properties obtained from the experimental (EXP) and numerical simulation (CFD)

	$\delta$ (mm)		$\delta^*$ (mm)	
	EXP	CFD	EXP	CFD
Suction surface	6.02	5.58	1.53	1.45
Pressure surface	17.01	15.80	2.59	2.67
average	11.52	10.69	2.06	2.06

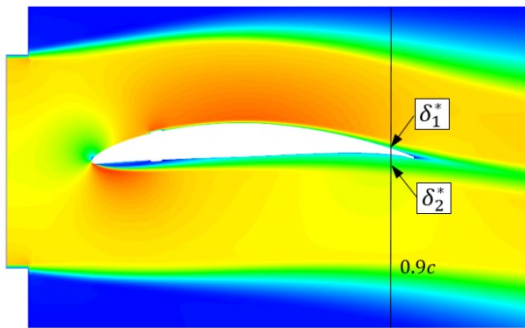


(a) aerofoil pressure surface

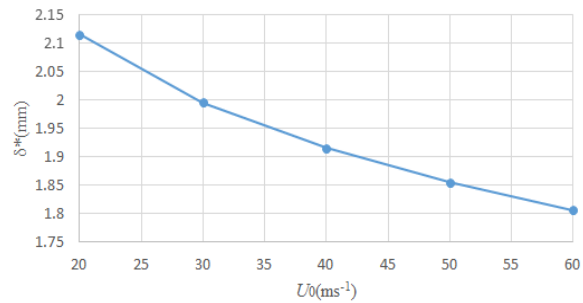


(b) aerofoil suction surface

**Fig. 6.** Results of the grid sensitivity study:  $2.4 \times 10^5$  nodes (case 1),  $3.9 \times 10^5$  nodes (case 2), and  $5.8 \times 10^5$  nodes (case 3)



(a)



(b)

**Fig. 7.** (a) Streamwise velocity contour, and the position for the determination of the averaged-boundary layer displacement thickness, and (b) distribution of the averaged-boundary layer displacement thickness against the inflow velocity  $U_o$

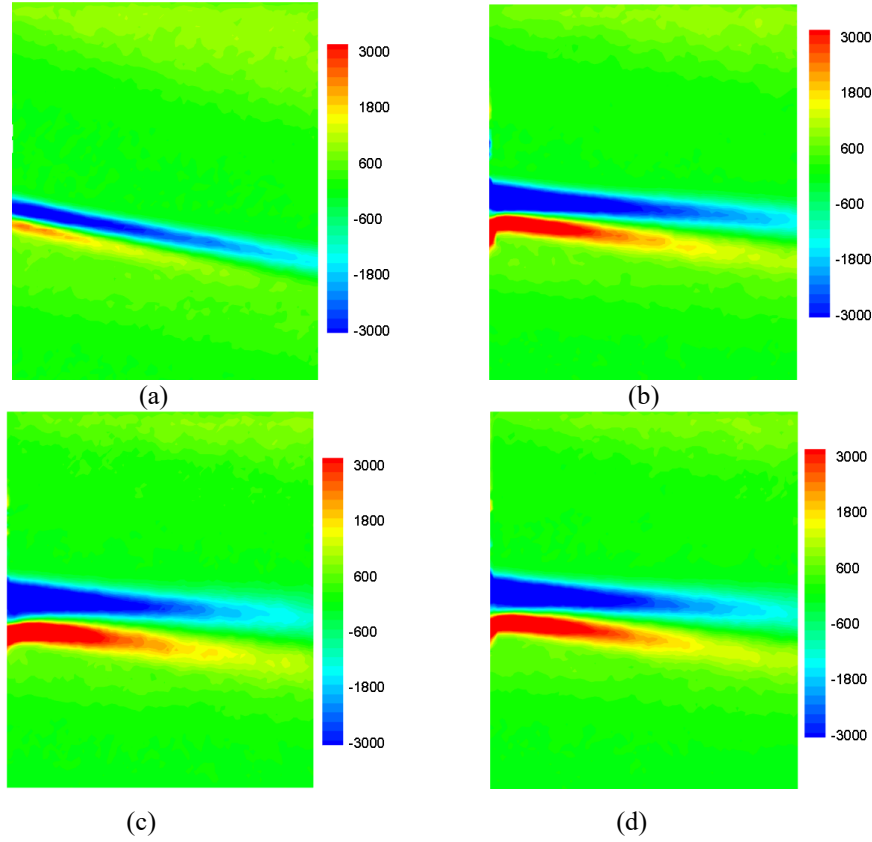


**Fig. 8.** The spanwise vorticity of the wake for fourth case: (a) baseline; (b) 30%–0.6mm; (c) 30%–1mm; (d) 30%–2mm

### 3. Flow field investigation

In this section, analysis of the measured flow-fields for the porous trailing edges 30%–1mm, 30%–2mm, 30%–0.6mm, as well as the baseline solid trailing edge, are provided. In order to investigate whether the wake flow can be altered by the porous trailing edges, the spanwise vorticity ( $\partial v/\partial x - \partial u/\partial y$ ) and velocity fluctuation fields produced by the porous trailing edges are investigated and compared against the baseline trailing edge. The analysis is performed in the  $X - Y$  coordinate system. Note that  $u$  and  $v$  are the longitudinal and wall-normal mean velocities, respectively.

The contours of the spanwise vorticity for the four cases are shown in Fig. 8. The inflow velocity is set at  $36 \text{ ms}^{-1}$ . The wake flow is characterised by two spanwise rollers of different rotating directions. These rollers come from the suction and pressure sides, respectively. For the baseline trailing edge, both rollers exhibit a downwash tendency due to the camber line of the aerofoil. In addition, the spanwise

vorticity level pertaining to the suction side roller is larger than that on the pressure side. Interestingly, the introduction of porous trailing edge will introduce several changes of the spanwise vorticity field. First, the spanwise rollers for both the suction and pressure sides increase in size and level, but it is more significant for the pressures side. Second, the downwash experienced by both rollers becomes less severe, where both rollers move towards the suction side of the aerofoil. The combination of the two phenomena implies that there might exist a cross-flow, which can only be facilitated by the porous channel upstream of the trailing edge at  $X < 0$ .

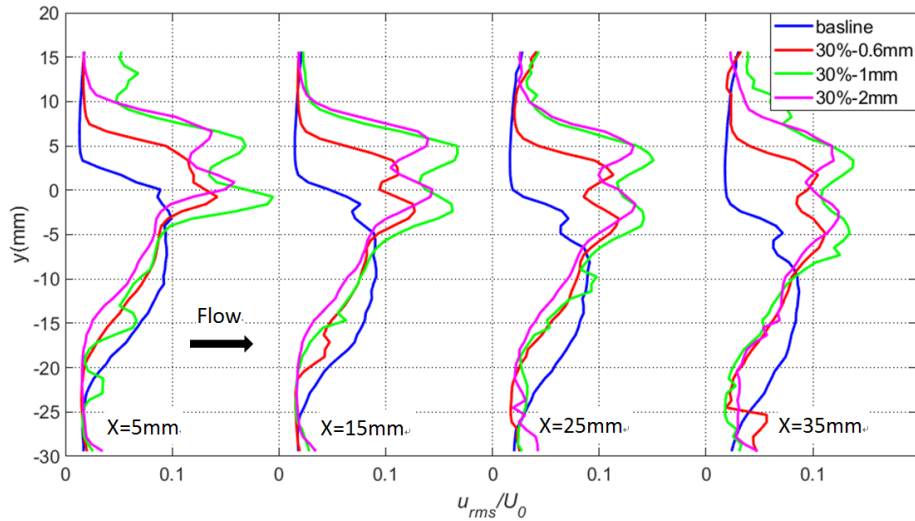


**Fig. 9.** Variation of the wake wall-parallel velocity profiles ( $u_{rms}/U_0$ ) at different  $X$  locations

The profiles of the root-mean-square (r.m.s.) of the longitudinal velocity normalised by the local freestream velocity,  $u_{rms}/U_0$ , at  $X = 5\text{mm}$ ,  $15\text{mm}$ ,  $25\text{mm}$  and  $35\text{mm}$ , are plotted in Fig. 9 for the four trailing edges. For the baseline trailing edge, two peaks can be identified that correspond to the buffer zones of the upstream turbulent boundary layers on the suction and pressure sides, respectively. The turbulence profiles pertaining to the baseline trailing edge also demonstrate the much thicker turbulent boundary layer thickness at the pressure side, which corroborates well with the numerical flow field in Fig. 7a. For the porous trailing edges, two distinct peaks of  $u_{rms}/U_0$  in the wake are demonstrated prominently. These peaks are much larger in the turbulence level than those of the baseline, whose wake profiles are already pertinent to a fully-developed turbulent boundary layer. In other words, the significantly elevated turbulence level of the wake flows by the porous trailing edges must be caused by some fluid phenomena other than the classical turbulent wake. It is also noteworthy that the double peaks of  $u_{rms}/U_0$  for the porous trailing edges migrate toward the suction side. This again suggests the presence of the cross-flow from the pressure side to the suction side that causes a global shift of the wake

development. Of all the porous trailing edges tested here, the largest increase in the turbulence level is measured for the case of 30%–1mm. The value of  $u_{rms}/U_0$  for 30%–1mm is almost twice that of the baseline trailing edge at  $X = 5\text{mm}$ . On the other hand, the case of 30%–0.6mm is the closest to the baseline trailing edge.

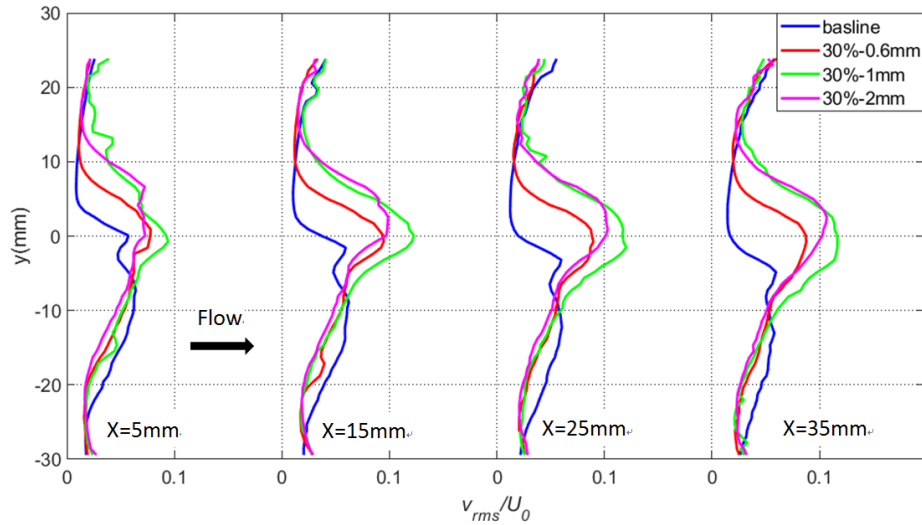


**Fig. 10.** Variation of the wall-normal wake velocity profiles ( $v_{rms}/U_0$ ) at different  $X$  locations

Fig. 10 shows the corresponding profiles of the r.m.s. wall-normal velocity fluctuations  $v_{rms}/U_0$ . The observation is quite similar to the  $u_{rms}/U_0$  counterpart: the porous trailing edges allow a general increase of  $v_{rms}/U_0$  with respect to the baseline trailing edge. Again, the level of increase is the largest for the 30%–1mm porous trailing edge, while the lowest level of increase belongs to the 30%–0.6mm porous trailing edge. The porous trailing edges also reduce the tendency of downwash.

It is noteworthy that, similar to the current results, previous investigation on the porous trailing edge of an asymmetric aerofoil by Moßner and Radespiel [33] also observe an increase of the r.m.s. velocity fluctuations at the suction side above the porous treatment. This result might be due to the imbalance of static pressure between the suction and pressure side of the trailing edge caused by the incidence. This can lead to a steady cross-flow blowing within the porous trailing edge, and cause an increase of the turbulence intensity in the wake especially at the suction side. However, the cross-flow blowing itself, which will be prominent only on the suction side, cannot explain the significantly enhanced double peaks of the  $u_{rms}/U_0$  and  $v_{rms}/U_0$  profiles observed in the current study. When we corroborate with the noise results to be discussed in the later sections, there are strong evidences that the enhanced double peaks of the  $u_{rms}/U_0$  and  $v_{rms}/U_0$  profiles by the porous trailing edges are due to the presence of the wake vortex shedding phenomenon. This unsteady fluids motion is well known to radiate significant level of

narrowband tone into the far field. The 30%–1mm porous trailing edge that produces the largest turbulence level in the wake profile indeed radiates the largest and the “sharpest” narrowband tone noise (Type 1) to the far field; whereas the 30%–0.6mm, whose turbulence level in the wake profile is the lowest amongst the porous trailing edges, can largely avoid the tone noise radiation. The 30%–2mm, whose turbulence levels between the above two, would radiate a more broadened tonal noise (Type 2).

#### 4. Discussion of the noise results

Acoustic measurements are mostly conducted at zero degree angle of attack of the aerofoil. The inflow velocity  $U_o$  varies between 20 and 60  $\text{ms}^{-1}$ . Fig. 11 shows examples of the  $PWL$  for the baseline aerofoil at different inflow velocities. The background noise is also included in the figure for comparison. It can be seen that the trailing edge self-noise level is well above the background noise level across almost the entire frequency range of interest.

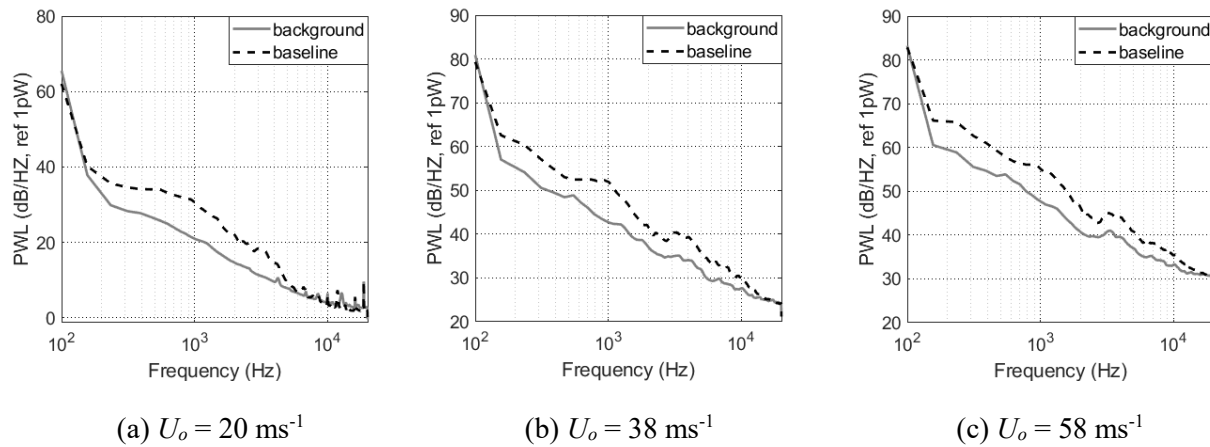
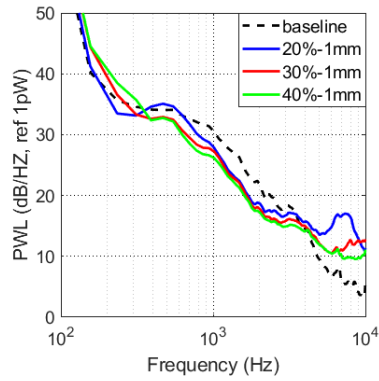


**Fig. 11.** Comparison of the  $PWL$  spectra produced by the baseline aerofoil at different inflow velocities

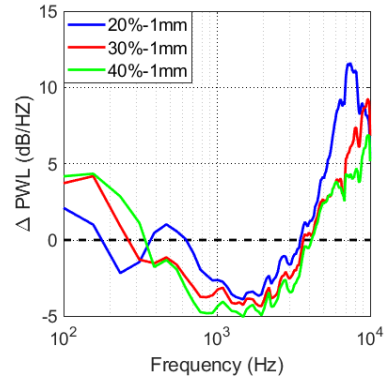
$U_o$

Unbeknown to the authors, and due to the lack of published literatures for guidance, the initial choices of  $d$  {1, 2, 3 mm},  $\sigma$  {20, 30, 40%} and  $\psi = 20\%$ , c.f. Table 1 for the wall-normal permeable trailing edges have a tendency to produce the narrowband tone in the acoustic spectra. This unwanted noise is especially prominent between the medium and large inflow velocity. The tone noise is generated by the periodic but unsteady wake structure due to the presence of pore-depth in the trailing edge. In what follows, Section 4.1 will discuss the effect of porous parameters in Table 1 on the turbulent broadband noise reduction at low inflow velocity condition that does not trigger the wake vortex shedding. Section 4.2 will discuss the effect of the porous parameters in Table 1 on the acoustic performance across the

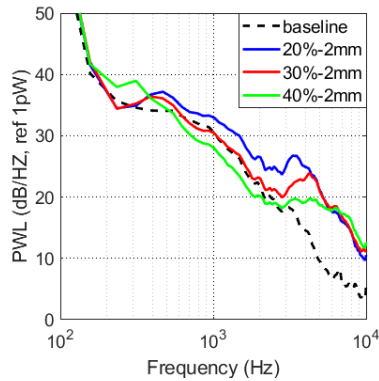
entire velocity range. In this section, attempt will also be made to non-dimensionalise the tone frequency by the porous geometrical parameters. Section 4.3 will non-dimensionalise the turbulent broadband noise frequency based on the calculated boundary layer displacement thicknesses. The effects of the different porous-coverages on the vortex shedding narrowband noise and turbulent broadband noise will be discussed in Section 4.4. The result of a sub-millimetre porous trailing edge whose porous configuration is shown in Table 3 is investigated in Section 4.5.



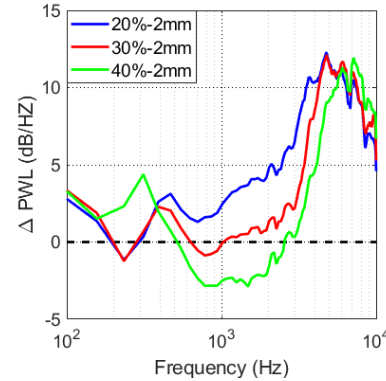
(a)



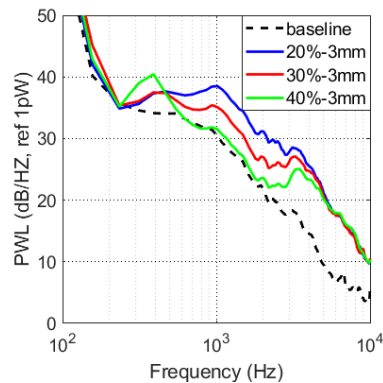
(b)



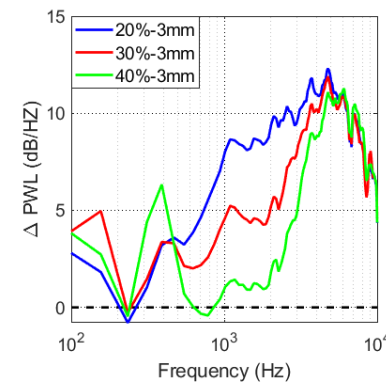
(c)



(d)



(e)



(f)

**Fig. 12.** (a, c, e)  $PWL$  spectra, and (b, d, f)  $\Delta PWL$  spectra at  $U_o = 20 \text{ ms}^{-1}$  produced by the porous trailing edges listed in Table 1 (different pore-sizes and porosities)

#### 4.1 Effect of the porous parameters in Table 1 to the turbulent broadband noise reduction at low inflow velocity

The  $PWL$  spectra produced by the porous trailing edges of pore-size  $d = 1 \text{ mm}$ , against porosity  $\sigma = 20, 30$  and  $40\%$  at  $U_o = 20 \text{ ms}^{-1}$  are presented in Fig. 12a. Fig. 12b shows the corresponding difference in the sound power level ( $\Delta PWL$ ) between the treated aerofoil and baseline aerofoil. According to Eq. (3), negative value of the  $\Delta PWL$  denotes noise reduction achieved by the porous trailing edge. The opposite is true for a positive value of the  $\Delta PWL$  means that the porous trailing edge produces larger level of  $PWL$  than the baseline trailing edge. It is interesting to note that the porous trailing edge distributed with relatively small pore-size can already produce quite a significant difference in the acoustical behaviours compared to the solid baseline trailing edge. For the most part, there is reduction of the turbulent broadband noise at around  $300 < f < 4000 \text{ Hz}$ . The level of noise reduction by the porous trailing edges improves when the porosity  $\sigma$  is increased. For the  $20\%–1\text{mm}$ ,  $30\%–1\text{mm}$  and  $40\%–1\text{mm}$  porous trailing edges, the maximum noise reduction of 3.5, 4.7 and 5.1 dB, respectively, can be achieved at the same frequency  $f \approx 1.5 \text{ kHz}$ . However, noise increase (i.e.  $\Delta PWL > 0$ ) can also be observed at frequency  $f > 4 \text{ kHz}$ . The level of noise increases can also be affected by the porosity. The increase in the noise level will become more significant when the porosity level is low.

Considering the  $20\%–1\text{mm}$ ,  $30\%–1\text{mm}$  and  $40\%–1\text{mm}$  porous trailing edges, the pore-size for them is the same. Therefore, a higher porosity among them denotes that (I) there are more pores per unit area, and (II) the values of  $t$  and  $h$  are smaller, i.e. the pores are closer to each other. Wall-normal permeable air through each pore into the boundary layer can be interpreted as a localised disturbing point to the turbulence. Because the spanwise turbulence correlation length scale is an important source for the broadband noise radiation at the trailing edge [34], it might be logical to link (I) & (II) as one of the mechanisms for the improved turbulent broadband noise reduction at  $300 < f < 4000 \text{ Hz}$  by higher porosity. Although we did not measure the spanwise correlation length in the current study, the reference to the relative difference should still be valid. In addition, the flow structures passing from one hole to the other are self-excited in a sort of turbulent motion similar to roughness. An increase of porosity that produces the effects of (I) & (II) would entail more spatial distribution of the permeable air through the pores. This phenomenon might create a synthetic surface roughness effect for the turbulent boundary layer, and ultimately increase the level of noise radiation at high frequency. Based on the results presented thus far, at first it seems counter-intuitive that a high porosity trailing edge does not suffer too much from the noise increase at  $f > 4 \text{ kHz}$ . However, one should also consider the effect of the pores on the other side of the trailing edge. Therefore, it is not straightforward to correlate the porosity to the noise radiation at

high frequency because it also depends on the boundary layer development at the pressure side of the aerofoil trailing edge. The sensitivity of the boundary layer to the different pressure loadings will also play a role. The situation can be exacerbated when the turbulent boundary layers on both sides of the trailing edge are very inhomogeneous, similar to the present NACA 65(12)-10 aerofoil where the turbulent boundary layer thickness at the pressure side is significantly larger than at the suction side of the baseline aerofoil (see Fig. 7a).

The  $PWL$  and  $\Delta PWL$  spectra produced by the porous trailing edges of  $d = 2$  and 3 mm, under the same range of porosity (20, 30 and 40%), are shown in Fig. 12(c, d) and Fig. 12(e, f), respectively. A trend discernible from these figures is that the enlarged pore-size can cause a deterioration of the broadband noise reduction performance. For example, the 20%–3mm will experience predominantly noise increase at  $300 < f < 4000$  Hz. This is in contrast with the 20%–1mm when it can actually achieve significant noise reduction at the same frequency range. Interestingly, at  $d = 2$  mm, a descending order for the porosity level from 40, 30 and 20% will trigger a transition for the  $\Delta PWL$  at the same frequency range to register  $< 0$ ,  $\approx 0$ , and  $> 0$ , respectively. Overall, the worst combination is those with large  $d$  and small  $\sigma$ . The noise increase at high frequency in Fig. 12(c, d) and Fig. 12(e, f) behaves similarly, where up to 10 dB can be observed at  $f > 4000$  Hz. A final point to make is that, for the porous trailing edge with  $d = 3$  mm, there is almost no noise reduction capability regardless the level of the porosity implemented. In Fig. 12(e, f), a tone-like feature with peak frequency at  $f \approx 1.1$  kHz for  $\sigma = 20, 30$  and 40% begins to emerge. This tonal peak could be an indication of the generation of the vortex shedding. The generation mechanism of these tonal peaks has already been reflected in Section 3 earlier. Further discussion on the tonal characteristics will be conducted in the Section 4.2.

#### 4.2 Using the porous geometrical parameters (Table 1) for the acoustical characterisation of the vortex shedding tones against a wide range of inflow velocity

For the porous trailing edges listed in Table 1, as well as the baseline trailing edge, the radiated  $PWL$  spectra are now measured across a large range of inflow velocity at  $20 \leq U_o \leq 60$  ms<sup>-1</sup>. The results are summarised in Fig. 13. It can be seen that, starting from  $U_o = 28$  ms<sup>-1</sup>, the  $PWL$  spectra is characterised by two types of tone radiation, depending on the combination of the pore-size  $d$ , and the porosity  $\sigma$ . Type 1 has a distinct sharp tone accompanied by a number of harmonics. These are highlighted in the sub-figures with a grey colour background. Type 2 has a broadened tonal-hump feature, and the harmonics are not as prominent. The associated sub-figures for the Type 2 are distinguishable in a white colour background. After extensive analysis of the large dataset, the frequencies pertaining to the sharp tones (Type 1) and tonal-hump (Type 2) are transformed into dimensionless form  $f'$  by the following:

$$\begin{aligned}
\text{(Type 1)} \quad f' &= \left(\frac{h}{d}\right)^2 \frac{f \cdot t_h}{U_o} & \frac{h}{d}, \frac{t}{d} &\leq 1.5 \\
\text{(Type 2)} \quad f' &= \frac{f \cdot t_h}{U_o} & \frac{h}{d}, \frac{t}{d} &> 1.5
\end{aligned} \tag{6}$$

where  $t_h$  is the most critical pore-depth, usually corresponds to the pores that are the furthest away from the trailing edge in the upstream direction. Pore-depth refers to the connecting vertical distance between both ends of the pore. When presence, it creates an effect that is analogous to a trailing edge bluntness.

In Eq. (6), the geometrical parameter that can differentiate the radiated tone from Type 1 to Type 2 is related to the  $h/d$  and  $t/d$ . A low value of  $h/d$  (achieved by either a low  $h$ , and/or a large  $d$ ) will entail the adjacent large-sized pores to be physically closer against each other in the spanwise direction. The geometrical characteristic of a low  $h/d$  is therefore a better resemblance to a two-dimensional blunt trailing edge. As a result, vortex shedding triggered by these pores is expected to be coherent in the spanwise direction, hence a better efficiency in the radiation of the sharp tones as underpinned by the wake profiles with the largest turbulence level for the double peaks in Figs. 8–10. However, the frequency scaling in Eq. (6) also stipulates that the corresponding Strouhal number needs an extra factor of  $(h/d)^2$  in order to collapse all the Type 1 main tones to  $f' = 0.17\text{--}0.18$ . For the Type 2 tone radiation, which is associated with the condition of  $h/d > 1.5$ , a conventional Strouhal number definition without the extra factor is already sufficient to describe the tonal-hump peak frequency, which all collapse at  $f' \approx 0.13$ . Table 5 tabulates the  $f'$  for both the Type 1 and Type 2 tones under several combinations of  $d$  and  $\sigma$ .

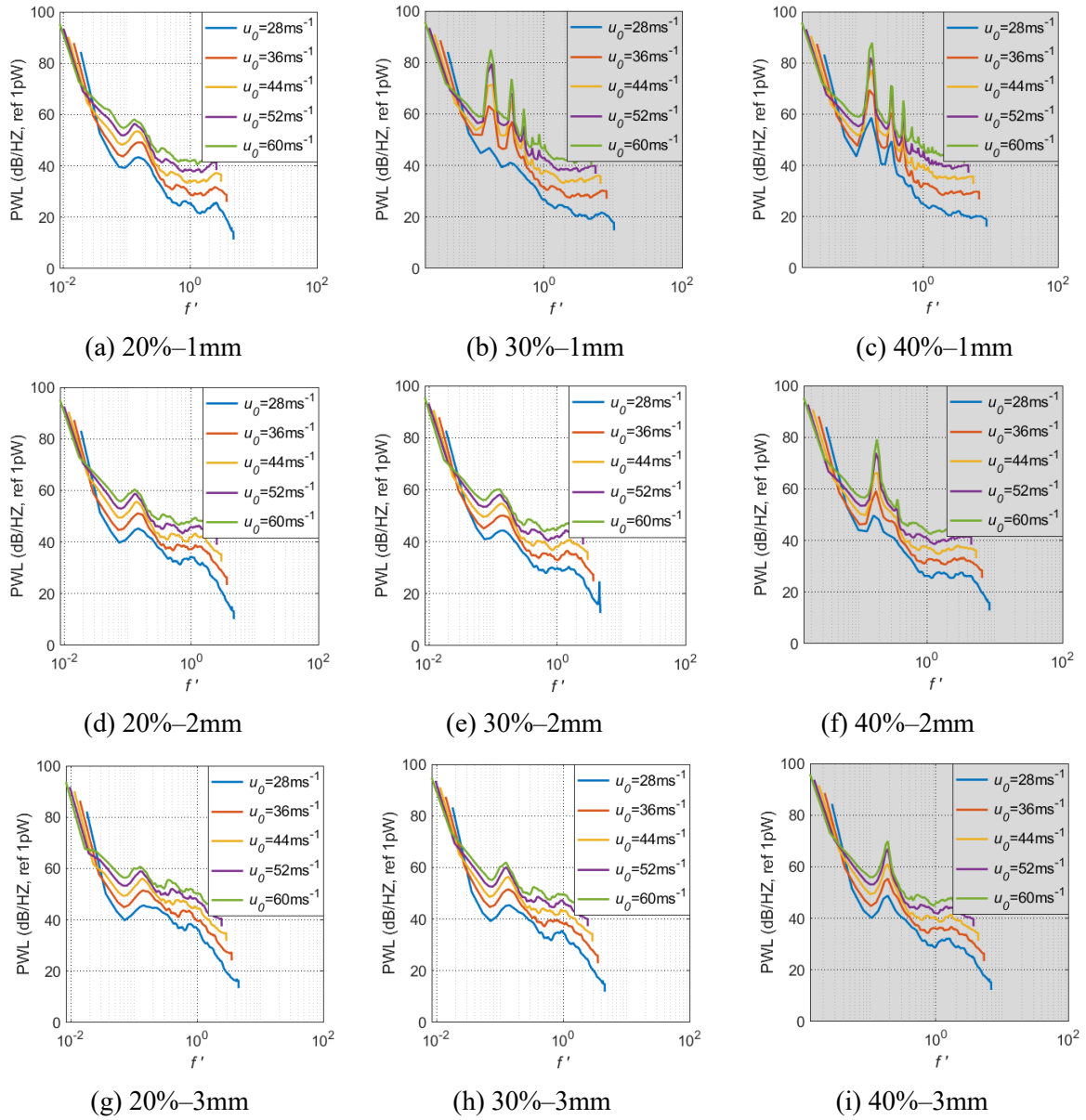


**Fig. 13.** *PWL* spectra against  $f'$  at  $U_o \geq 28 \text{ ms}^{-1}$  produced by porous trailing edges listed in Table 1 (different pore-sizes and porosities)

**Table 5** Tabulated values of  $f'$  produced by the Type 1 tones (grey background) and Type 2 tones.

	$d = 1$ mm				$d = 2$ mm		$d = 3$ mm
	Tonal peak				Tonal peak		Tonal peak
	First	Second	Third	Fourth	First	Second	First
$\sigma = 20\%$	0.1326				0.1277		0.1248
$\sigma = 30\%$	0.1713	0.3414	0.5127	0.6839	0.1285		0.1248
$\sigma = 40\%$	0.1752	0.3503	0.5096	0.6848	0.1841	0.3681	0.1851

Equation (6) is derived empirically from a large database of *PWL* spectra where all the wall-normal permeable trailing edges are configured to the same porous-coverage of  $\psi = 20\%$ . Obviously, the values of  $t_h$  will be very similar for all the porous trailing edges listed in Table 1. One may then question whether Eq. (6) is applicable to other wall-normal permeable trailing edges whose the porous-coverage  $\psi$ , and subsequently the most critical  $t_h$  will be different. To investigate this, some of the porous trailing edges listed in Table 2 will be used. In Table 2, the porous trailing edges all have the same geometrical characteristics:  $d = 1$  mm,  $\sigma = 30\%$  and  $t = h = 1.5$  mm. However, they are different in the porous coverage  $\psi$  and the critical  $t_h$ . For  $\psi = 11.7\%$ ,  $13.7\%$  and  $15.7\%$ , the corresponding  $t_h = 3.9$ ,  $4.6$  and  $5.3$  mm, respectively. The three porous trailing edges are chosen to verify the Eq. (6). The radiated *PWL* spectra are measured at inflow velocities between  $20 \leq U_o \leq 60$   $\text{ms}^{-1}$ , and the results are presented in Fig. 14. The combination of  $d$  and  $\sigma$  for these porous trailing edges suggests that the radiated tone should belong to Type 1, which is indeed manifested accurately in the figures. Interestingly, all the main tones also collapse at  $f' = 0.17\text{--}0.18$ . Summary of these non-dimensional frequencies can be found in Table 6. The results confirm that Eq. (6) is indeed universal, and is versatile for the prediction of the vortex shedding tone frequency produced by a wall-normal permeable trailing edge. Fig. 14 also reflects an interesting phenomenon. Under the same inflow velocity (e.g. take the  $U_o = 36$   $\text{ms}^{-1}$ ), one can observe the transition from a minor tone radiation to a high amplitude sharp tone when the  $\psi$  increases from  $11.7\%$  to  $13.7\%$ , and then to  $15.7\%$ . This indicates that the radiated tone noise amplitude is a function of the critical  $t_h$ , and is very likely to be related to the strength of the wake vortex shedding.

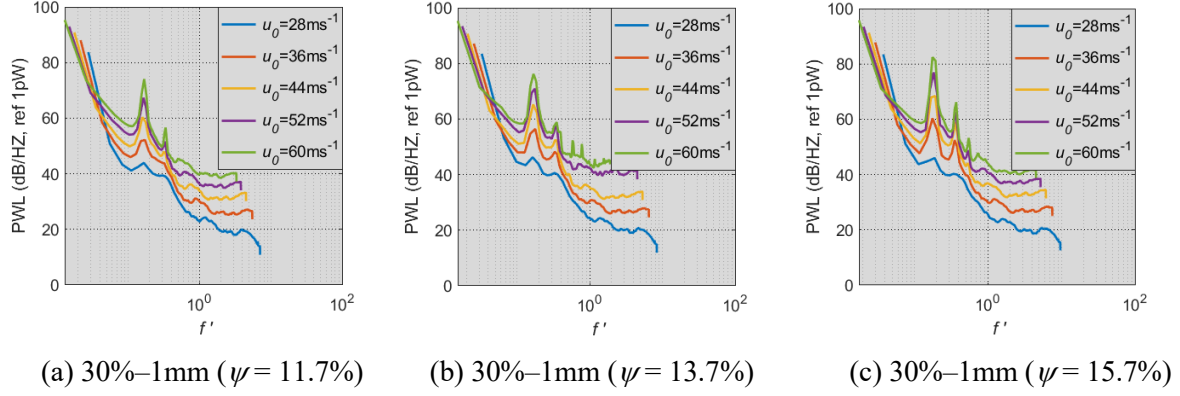


**Fig. 14.** *PWL* spectra against  $f'$  at  $U_o \geq 28 \text{ ms}^{-1}$  produced by porous trailing edges listed in Table 2 (different porous-coverages)

**Table 6** Tabulated values of  $f'$  for  $\sigma = 30\%$ ,  $d = 1 \text{ mm}$  at different rows

$d = 1 \text{ mm}$ , Porosity=30%				
	Tonal noise peak			
	First	Second	Third	Fourth
$\psi = 11.7\%$	0.1677	0.3354		
$\psi = 13.7\%$	0.1679	0.3511	0.5801	
$\psi = 15.7\%$	0.1767	0.371	0.5477	0.742

#### 4.3 Using the boundary layer parameters for the acoustical characterisation of the turbulent broadband noise against a wide range of inflow velocity

So far, analysis in the previous section focuses on the characterisation of the vortex shedding tone noise only. Next, the investigation will shift the focus on the effect of pore-size  $d$  on the reduction of the turbulent broadband noise. The frequency pertaining to the turbulent broadband noise will be non-dimensionalise in the form of Strouhal number by the turbulent boundary layer displacement thicknesses  $\delta^*$ . Fig. 15 shows the contours of  $\Delta PWL$  produced by the porous trailing edges of various  $d$  at a fixed  $\sigma = 30\%$ , against non-dimensional frequency of  $f\delta^*/U_o$ , at four inflow velocities  $U_o = 20, 30, 40$  and  $50 \text{ ms}^{-1}$ . Note that the  $\delta^*$  at each  $U_o$  is obtained by the procedure described in Section 2.4. The upper and lower limits of the colour scale are set at  $\pm 5 \text{ dB}$  in order to emphasise a detailed transition in the  $\Delta PWL$  at the frequency range that corresponds to the turbulent broadband noise radiation.

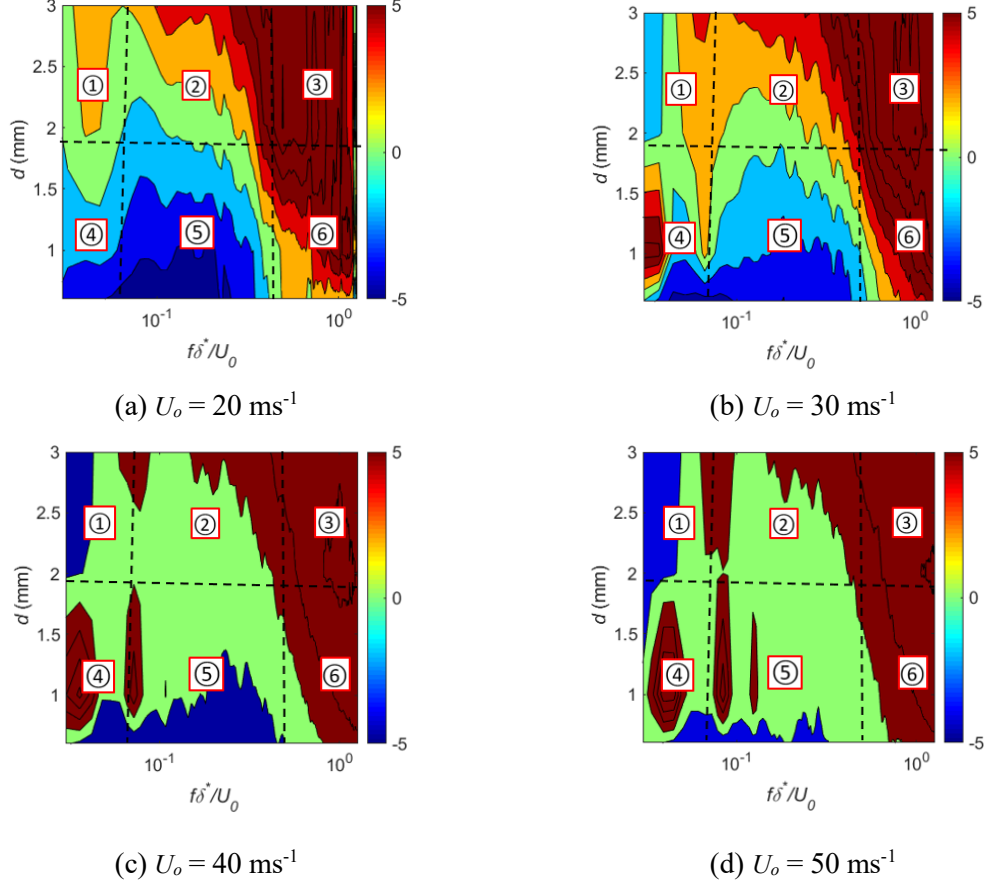


**Fig. 15.**  $\Delta PWL$  (dB) spectra produced by the porous trailing edges of different pore-size  $d$  against  $f\delta^*/U_o$  at different inflow velocities  $U_o$ . The porosity is fixed at  $\sigma=30\%$

Due to the dominance of the vortex shedding noise at higher  $U_o$  for almost all the porous trailing edges tested in Table 1, it is not surprised that the figures cannot maintain a coherent  $\Delta PWL$  characteristic across the inflow velocity range. The only exception is that all the porous trailing edges would experience noise increase at the high frequency (zones 3 and 6 in all the figures) regardless the choice of the pore-size  $d$ . Before the occurrence of the Type 1 and Type 2 tone noise at  $U_o \leq 30 \text{ ms}^{-1}$ , there is almost no noise reduction effect when  $d \geq 2 \text{ mm}$  (Fig. 15a and 15b, zones 1, 2 and 3). Instead, the turbulent broadband noise reduction only occurs in the low and middle frequency range for  $d < 2 \text{ mm}$  (Fig. 15a and 15b, zones 4 and 5). At  $U_o \geq 40 \text{ ms}^{-1}$ , the  $\Delta PWL$  is close to zero in zones 2 and 5 (Fig. 15c and 15d). The effect of the pore-size on the  $\Delta PWL$  at the low frequency zones (1 and 4), as the function of  $U_o$ , can be quite interesting. For  $d \geq 2 \text{ mm}$ , noise reduction can be achieved at zone 1, which becomes more prominent as the  $U_o$  increases. Conversely, at  $d < 2 \text{ mm}$ , the initial noise reduction in zone 4 will slowly be superseded by the noise increase as the  $U_o$  increases.

A general picture on the acoustical response of the porous trailing edges described in [Table 1](#) has now been built up. The vortex shedding tones (both Type 1 and Type 2) could be a prominent feature for the wall-normal permeable trailing edges. The optimal combination of  $\sigma$  and  $d$  to minimise this extraneous noise source seems to be referring to a small  $\sigma$  and small  $d$ . For the turbulent broadband noise, the optimal configuration for the reduction is the combination of large  $\sigma$  and small  $d$ , but this combination is only limited to  $U_o \leq 30 \text{ ms}^{-1}$ . The pore-size  $d$  can be regarded as the first-order parameter for the aeroacoustics responses for the porous trailing edges. This is because it can be so sensitive that a slight increase in  $d$ , regardless of the porosity level, could jeopardise the aeroacoustics performance significantly in both the frequency and inflow velocity domains.

#### 4.4 Effects of the porous-coverage ([Table 2](#)) on the radiated self-noise spectra

In order to investigate the effect of porous-coverage  $\psi$  to the radiated trailing edge noise, 17 different levels of porous-coverage, all of which are configured by  $d = 1 \text{ mm}$ ,  $\sigma = 30\%$ ,  $t = h = 1.5 \text{ mm}$ , circular pore-shape and rectilinear pore-pattern, are investigated for their aeroacoustics behaviours. It should be noted that possessing different porous-coverage will entail different critical thickness  $t_h$  for the porous trailing edges. It is important to remind again that the porous-coverage starts from the trailing edge and counts towards the upstream direction. The larger value of the porous-coverage, the larger portion of the trailing edge is covered by the wall-normal permeability. The readers are directed to the parameters listed in [Table 2](#) for the detailed geometrical information.

After analysing all the dataset, the presence of the vortex shedding is found to correlate well with the local  $\delta^*$ , and the critical thickness  $t_h$  (i.e. the furthest upstream porous row). It is found that the vortex shedding tone noise (both Type 1 and Type 2) will occur when the following condition is satisfied:

$$t_h/\delta^* \geq 2 \quad (7)$$

Note that  $\delta^*$  used here corresponds to the averaged turbulent boundary layer displacement thickness for the suction and pressure sides at the same streamwise location as the  $t_h$ . [Equation \(7\)](#) represents a useful condition to predict the initialisation of the bluntness-induced tone noise under a specific combination of the wall-normal permeable geometry and boundary layer development.

[Fig. 16](#) presents the *PWL* spectra produced by different porous-coverages: 30%–1mm ( $\psi = 3.7\%$ ), 30%–1mm ( $\psi = 6.7\%$ ) ... 30%–1mm ( $\psi = 15.7\%$ ), at  $U_o = 20, 30$  and  $40 \text{ ms}^{-1}$ . It clearly shows that the turbulent broadband noise reduction can be achieved at  $U_o = 20 \text{ ms}^{-1}$  at  $f < 4 \text{ kHz}$  for all the porous-coverage configurations, including the 30%–1mm ( $\psi = 3.7\%$ ) which has the least amount of porous treatment. The level of turbulent broadband noise reduction increases when the number of porous-

coverage is increased. However, at  $f \geq 6$  kHz, the reverse happens. The level of high frequency noise increase is now enhanced by the trailing edge with larger value of the porous-coverage. Such opposite trend is attributed to the “double-edged sword” of the permeable flows, where a favourable effect of mixing and dissipating the turbulent boundary layer, hence reduction of the self-noise radiation is negated by the adverse effect of the increased synthetic surface roughness to cause a high frequency noise increase.

At the higher inflow velocities, e.g.  $U_o = 30$  and  $40 \text{ ms}^{-1}$ , the extraneous tone noise generated by the vortex shedding will start to occur at low frequency when  $\psi \geq 6.7\%$ . The tone noise becomes more significant as the  $\psi$  increases. This trend is expected because a large  $\psi$  is associated with (1) a large value of the  $t_h$ , and (2) a lower value of the  $\delta^*$ . The combination of the two will make it easier to fulfill the condition in Eq. (7). In addition, the primary tone frequency is pushed towards the lower frequency when  $\psi$  increases. This reflects the Strouhal number rule, where all the bluntness-induced tone noise can be predicted accurately by the empirical equation of Eq. (6). Across the frequency range up to 6 kHz, when the permeable trailing edges with low values of  $\psi$  are not masked by the extraneous tone noise, the corresponding *PWL* spectra will always exhibit turbulent broadband noise reduction. Therefore the 30%–1mm ( $\psi = 3.7\%$ ) trailing edge represents a very good choice. This is because with this configuration even at high inflow velocity there is still lack of mechanism to generate the vortex shedding tone noise (see Eq. 7), whilst good level of turbulent broadband noise reduction can always be ensured. Although not measured in the current study, it is also expected that the 30%–1mm ( $\psi = 3.7\%$ ) trailing edge will incur the least aerodynamics penalty amongst the others due to the least level of porous-coverage at the trailing edge.

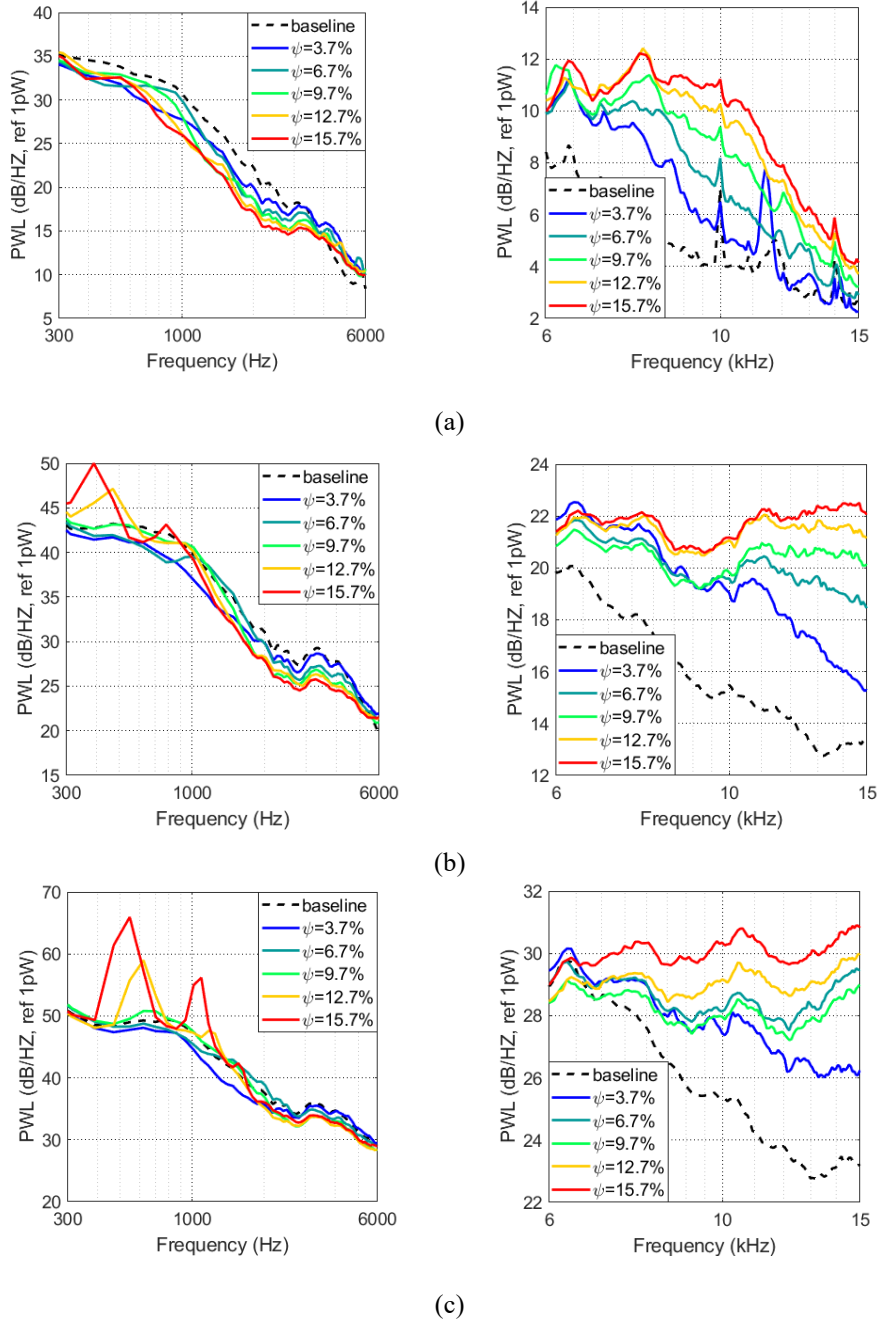


**Fig. 16.** *PWL* spectra against frequency at (a)  $U_o = 20 \text{ ms}^{-1}$ , (b)  $U_o = 30 \text{ ms}^{-1}$ , (c)  $U_o = 40 \text{ ms}^{-1}$  produced by porous trailing edges listed in Table 2 (different porous-coverages). The pore-size and porosity for these trailing edges are fixed at  $d = 1 \text{ mm}$  and  $\sigma = 30\%$ , respectively

#### 4.5 Effect of the porous parameters in Table 3 for the turbulent broadband noise reduction

Although the 30%–1mm ( $\psi = 3.7\%$ ) has previously been identified as a good choice, it still has some limits to achieve the highest value for the  $\Delta PWL$  in the turbulent broadband noise. Based on all the results presented thus far, some design criteria for an optimal wall-normal permeable porous trailing edge can now be established. Based on the  $\Delta PWL$  trend observed in Fig. 15, a sub-millimetre  $d$  accompanied by a medium porosity  $\sigma$  could be an ideal combination to avoid the vortex shedding tone noise and to achieve reduction of the turbulent broadband noise. In order to investigate the effect of a sub-millimetre porous trailing edge to the radiated trailing edge noise, the porous configuration tested here is  $d = 0.6$  mm,  $\sigma = 30\%$ ,  $\psi = 20\%$ , i.e. 30%–0.6mm, as summarised in Table 3.

Fig. 17 shows the contour of  $\Delta PWL$  as a function of  $f$  and  $U_o$  using the above configuration for a wall-normal permeable trailing edge. The figure clearly demonstrates that significant turbulent broadband noise reduction of up to 7 dB can be achieved across a wide range of frequency and inflow velocity. No vortex shedding tone noise is produced, except at  $U_o = 60$  ms<sup>-1</sup> where some footprints of the tone noise radiation can be observed. The level of noise increase at high frequency is also decreased significantly compared to all the other results presented up to now.

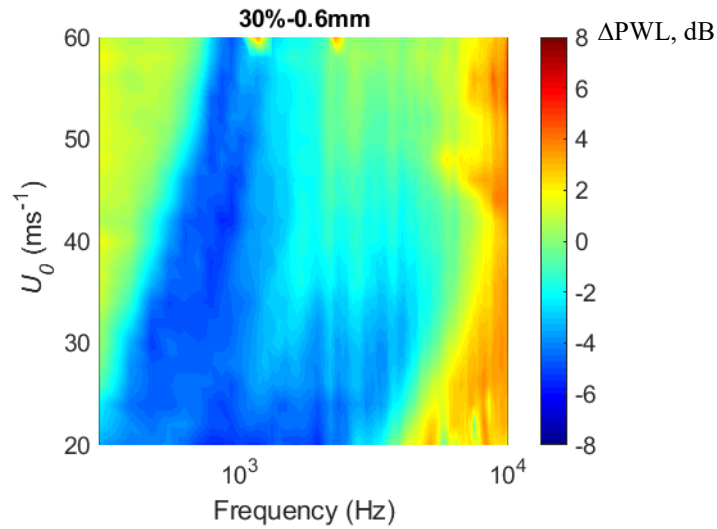


**Fig. 17**  $\Delta PWL$  (dB) contour in the inflow velocity and frequency domain produced by the sub-millimetre porous trailing edge listed in Table 3

## 5. Conclusions

The main aim of this research is the sensitivity and parametric study of the sound generation at the porous trailing edge of an aerofoil. Some design parameters for the porous properties include the porosity, pore-size, and porous-coverage at the trailing edge. These porous properties, especially for a wall-normal permeable structure, can be replicated easily by the additive manufacturing. The experiments were conducted in an aeroacoustics wind tunnel across chord-based Reynolds numbers between 0.2 and 0.6 million. The far-field measurements in an anechoic chamber of a very low background noise environment enable an accurate quantification of the sound power level radiated by the trailing edges.

A complementary flow-field measurement on the wake, subjected to the baseline trailing edge and three other types of porous trailing edges, has been conducted by the PIV technique. Generally, the introduction of the porous treatment on the trailing edge will cause a vivid footprint in the wake flow whereby a global upward shift of the wake shear layers (in relative to the wake flow produced by the baseline trailing edge) can be observed. This suggests that a cross-flow phenomenon has been facilitated by the porous channels at the trailing edge. Most importantly, the nominal turbulent wake suddenly undergoes a significant change to a new flow feature that contains significantly higher level of turbulence intensity. This flow feature indeed reminisces that of the vortex shedding. In what follows, summary of the noise results will be provided to corroborate with the flow results, and to confirm that the tone noise radiation observed in the acoustic spectra is indeed related to the vortex shedding phenomenon.

A significant number of the porous trailing edges are characterised by the appearance of both the sharp and broadened tones in the acoustic spectra. These extraneous features can be so dominant that some of them produce noise level higher than the baseline unmodified aerofoil across a large frequency range. Detailed investigation on the acoustical dataset reveals several patterns. First, both the sharp and broadened tones can only be produced if the most critical pore-depth of the porous trailing edge at least twice as large as the locally averaged turbulent boundary layer displacement thickness. Second, the parameter that dictates the radiation of the sharp tone or the broadened tone is the ratio between the distance of the adjacent pores and the pore-diameter. If this ratio is less than or equal to 1.5, sharp tones will be the dominant feature, and the opposite is true. Third, the frequency pertaining to either the sharp tone or the broadened tone is found to follow the Strouhal number relationship (when the most critical pore-depth is used as the length scale). This not only allows the prediction of the main tone frequency, but also confirms that the hydrodynamic source for these tones is indeed the wake vortex shedding. Generally, the production of the vortex shedding tone is prone to the porous parameters of large pore-size, small porosity and large porous-coverage.

If the vortex shedding tones can be avoided, the wall-normal permeable trailing edge becomes a very effective tool to reduce the turbulent broadband noise. For example, when the porous trailing edge with

sub-millimetre diameter is designed, it can completely suppress the vortex shedding tone noise, and at the same time improve the level of turbulent broadband noise reduction. In addition, the level of noise increase at high frequency can also be lessened by the use of small pore-size. The optimal combination of the porous parameters refers to small pore-size (sub-millimetre), and medium to large porosity.

The sensitivity of the self-noise radiation with respect to the porous-coverage for the trailing edge is another important finding. The presented results indicate that considerable reduction of the turbulent broadband noise can already be achieved with mere 3.7% coverage of the porous trailing edge. Further increase in the porous-coverage does improve the level of reduction for the turbulent broadband noise slightly, but the impact is much less than when a small pore-size trailing edge is used. This reflects that the main trailing edge noise source is only situated very near to the edge. Therefore, a targeted approach (i.e. small porous-coverage) not only is already sufficient to achieve significant trailing edge self-noise reduction, but also has a potential to incur smaller penalty in the aerodynamics performance.

## Acknowledgment

The first author would like to thank the financial support (Grant No. 0103014) provided by Shandong University of Science and Technology, China. We would also like to thank the PhD student Mr. Philip Woodhead from Brunel University London for providing some of the experimental data.

## References

- [1] [Air Travel – Annual Report on Greener by Design, Royal Aeronautical Society \(2018\).](#)
- [2] [E. Sarradj, C. Fritzsche, T. Geyer, Silent owl flight: Bird fly over noise measurements, AIAA Journal. 49 \(2011\) 769– 779.](#)
- [3] [A. Bodling, A. Sharma, Numerical investigation of noise reduction mechanisms in a bio-inspired airfoil, Journal of Sound and Vibration. 453 \(2019\) 314–327.](#)
- [4] [J. W. Jaworski, N. Peake, Aerodynamic noise from a poroelastic edge with implications for the silent flight of owls, Journal of Fluid Mechanics. 723 \(2013\) 456–479.](#)
- [5] [I. A. Clark, W. N. Alexander, W. Devenport, Bioinspired trailing-edge noise control, AIAA Journal. 55 \(2017\) 740-754](#)
- [6] [M. Gruber, Airfoil noise reduction by edge treatments. PhD dissertation, the University of Southampton, 2012.](#)

- [7] Z. Zuo, Q. Huang, S. Liu. An Analysis on the Flow Field Structures and the Aerodynamic Noise of Airfoils with Serrated Trailing Edges Based on Embedded Large Eddy Flow Simulations, *Journal of Applied Fluid Mechanics*. 12 (2019) 327-339.
- [8] D. J. Moreau, C. J. Doolan, The generation of tonal noise from sawtooth trailing-edge serrations at low Reynolds numbers, *The Aeronautical Journal*. 120 (2016) 971-983.
- [9] F. Avallone, W.C.P. van der Velden, D. Ragni, Benefits of curved serrations on broadband trailing-edge noise reduction, *Journal of Sound and Vibration*. 400 (2017) 167-177.
- [10] J. R. Mathews, N. Peake, An analytically-based method for predicting the noise generated by the interaction between turbulence and a serrated leading edge, *Journal of Sound and Vibration*. 422 (2018) 506–525.
- [11] A. S.H. Lau, S. Haeri, J. W. Kim, The effect of wavy leading edges on aerofoil–gust interaction noise, *Journal of Sound and Vibration*. 332 (2013) 6234–6253.
- [12] J. Gill, X. Zhang, P. Joseph, Symmetric airfoil geometry effects on leading edge noise, *The Journal of the Acoustical Society of America*. 134 (2013) 2669-2680.
- [13] A. Vathylakis, T.P. Chong, P.F. Joseph, Poro-serrated trailing-edge devices for airfoil self-noise reduction, *AIAA Journal*. 53 (2015) 3379–3394.
- [14] T.P. Chong, E. Dubois, Optimization of the poro-serrated trailing edges for airfoil broadband noise reduction, *Journal of the Acoustical Society of America*. 140 (2016) 1361–1373.
- [15] F. Avallone, W.C.P. van der Velden, D. Ragni, D. Casalino, Noise reduction mechanisms of sawtooth and combed-sawtooth trailing-edge serrations, *Journal of Fluid Mechanics*. 848 (2018) 560–591.
- [16] A. Wolf, T. Lutz, W. Würz, E. Krämer, O. Stalnov, A. Seifert, Trailing edge noise reduction of wind turbine blades by active flow control, *Wind Energy*. 18 (2015) 909–923.
- [17] T. A. Leitch, C. A. Saunders, W.F. NG, Reduction of unsteady stator-rotor interaction using trailing edge blowing, *Journal of Sound and Vibration*. 235 (2000) 235–245.
- [18] T. Geyer, E. Sarradj, C. Fritzsche, Measurement of the noise generation at the trailing edge of porous airfoils, *Experiments Fluids*. 48 (2010) 291–308.
- [19] T. Geyer. Trailing edge noise generation of porous airfoils. PhD dissertation, Brandenburg University of Technology Cottbus, 2011
- [20] T. Geyer, E. Sarradj, Noise generation by porous airfoils, In: 13th AIAA/CEAS Aeroacoustics Conference, 21-23 May 2007, Rome, Italy.
- [21] T. Geyer, E. Sarradj, Trailing edge noise of partially porous airfoils, In: 20th AIAA/CEAS Aeroacoustics Conference, 16-20 June 2014, Atlanta, USA.

- [22] M. Herr, K.S. Rossignol, J. Delfs, M. Mößner, N. Lippitz, Specification of porous materials for low-noise trailing-edge applications, In: 20th AIAA/CEAS Aeroacoustics Conference, 16-20 June 2014, Atlanta, USA.
- [23] A. R. Carpio, R. M. Martínez, F. Avallone, D. Ragni, M. Snellen, S. van der Zwaag, Experimental characterization of the turbulent boundary layer over a porous trailing edge for noise abatement, *Journal of Sound and Vibration*. 443 (2019) 537-558.
- [24] S. R. Koh, B. Zhou, M. Meinke, N. Gauger, W. Schröder, Numerical analysis of the impact of variable porosity on trailing-edge noise, *Computers and Fluids*. 167 (2018) 66–81.
- [25] S. R. Koh, M. Meinke, W. Schröder, Numerical analysis of the impact of permeability on trailing edge noise, *Journal of Sound and Vibration*. 421 (2018) 348-376.
- [26] B. Zhou, S. R. Koh, N. R. Gauger, M. Meinke, W. Schröder, A discrete adjoint framework for trailing-edge noise minimization via porous material, *Computers and Fluids*. 172 (2018) 97–108.
- [27] R. Hedayati, A. R. Carpio, S. Luesutthiviboon, D. Ragni, F. Avallone, D. Casalino, S. van der Zwaag, Role of polymeric coating on metallic foams to control the aeroacoustic noise reduction of airfoils with permeable trailing edges, *Materials*. 12 (2019) 1087-1100.
- [28] I. Gibson, D. Rosen, B. Stucker, *Additive Manufacturing Technologies*, Springer New York, New York, NY, 2015.
- [29] C. Jiang, Y. Yauwenas, J. Fischer, D. Moreau, C. Doolan, J. Gao, W. Jiang, R. McKay, M. Kingan, Control of rotor trailing edge noise using porous additively manufactured blades. In: 24th AIAA/CEAS Aeroacoustics Conference, 25-29 June 2018, Atlanta, Georgia, USA
- [30] A. R. Carpio, F. Avallone, D. Ragni, M. Snellen, S. van der Zwaag, 3D-printed perforated trailing edges for broadband noise abatement. In: 25th AIAA/CEAS Aeroacoustics Conference, 20-23 May 2019, Delft, Netherlands.
- [31] C. Wang, Trailing edge perforation for interaction tonal noise reduction of a contra-rotating fan, *Journal of Vibration and Acoustics*. 140 (2018) 1-14.
- [32] CK. Sumesh, T.J. S. Jothi, Aerodynamic noise characteristics of a thin airfoil with line distribution of holes adjacent to the trailing edge, *International Journal of Aeroacoustics*. 18 (2019) 496–516.
- [33] M. Moßner, R. Radespiel, Flow simulations over porous media: comparisons with experiments, *Computers and Fluids* 154 (2017) 358–370.
- [34] R Amiet, Noise due to turbulent flow past a trailing edge, *Journal of Sound and Vibration*. 47 (1976) 387–393.